Intrinsic defects and mid-gap states in quasi-one-dimensional indium telluride

Meryem Bouaziz, Aymen Mahmoudi, Geoffroy Kremer, Julien Chaste, César González, Yannick J. Dappe, François Bertran, Patrick Le Fèvre, Marco Pala, Fabrice Oehler, et al.

Intrinsic defects and mid-gap states in quasi-one-dimensional indium telluride

Meryem Bouaziz,[1,*] Aymen Mahmoudi,[1] Geoffroy Kremer,[1,2] Julien Chaste,[1] César González,[3,4] Yannick J. Dappe,[5] François Bertran,[6] Patrick Le Fèvre,[6] Marco Pala,[1] Fabrice Oehler,[1] Jean-Christophe Girard,[1] and Abdelkarim Ouerghi[1,†]

[1]*Université Paris-Saclay, CNRS, Centre de Nanosciences et de Nanotechnologies, 91120 Palaiseau, Paris, France*
[2]*Institut Jean Lamour, UMR 7198, CNRS-Université de Lorraine, Campus ARTEM, 2 allée André Guinier, BP 50840, 54011 Nancy, France*
[3]*Departamento de Física de Materiales, Universidad Complutense de Madrid, 28040 Madrid, Spain*
[4]*Instituto de Magnetismo Aplicado UCM-ADIF, E-28232 Las Rozas de Madrid, Spain*
[5]*SPEC, CEA, CNRS, Université Paris-Saclay, CEA Saclay, Gif-sur-Yvette Cedex 91191, France*
[6]*Synchrotron SOLEIL, L'Orme des Merisiers, Départementale 128, F-91190 Saint-Aubin, France*

(Received 20 February 2023; revised 19 May 2023; accepted 24 May 2023; published 5 September 2023)

Recently, intriguing physical properties have been unraveled in anisotropic semiconductors in which the in-plane electronic band structure anisotropy often originates from the low crystallographic symmetry. The atomic chain is the ultimate limit in material downscaling for electronics—a frontier for establishing an entirely new field of one-dimensional quantum materials. Electronic and structural properties of chain-like InTe are essential for a better understanding of device applications such as thermoelectrics. Here, we use scanning tunneling microscopy/scanning tunneling spectroscopy (STS) measurements and density functional theory (DFT) calculations to image the in-plane structural anisotropy directly in tetragonal InTe. As results, we report the direct observation of one-dimensional In^{1+} chains in InTe. We demonstrate that InTe exhibits a bandgap of about 0.40 ± 0.02 eV located at the M point of the Brillouin zone. Additionally, line defects are observed in our sample and were attributed to In^{1+} chain vacancy along the c-axis—a general feature in many other TlSe-like compounds. Our STS and DFT results prove that the presence of In^{1+} induces a localized gap state, located near the valence band maximum. This acceptor state is responsible for the high intrinsic p-type doping of InTe that we also confirm using angle-resolved photoemission spectroscopy.

DOI: 10.1103/PhysRevResearch.5.033152

I. INTRODUCTION

In the vast family of two-dimensional (2D) van der Waals materials [1], many iconic compounds such as graphene, boron nitride, or transition metal dichalcogenide (MX_2, with M being a transition metal and X a chalcogen element [2–4]) display a hexagonal crystal symmetry. Consequently, their out-of-plane (z direction) properties (e.g., electronic, mechanic, thermal) are usually very different from their in-plane counterpart (xy directions), but the material is essentially isotropic in the xy plane due to the six-fold crystal symmetry [5]. In addition to those 2D in-plane isotropic compounds, quasi-one-dimensional (quasi-1D) crystals are a class of anisotropic materials wherein atoms are arranged within the xy plane to form 1D-like structures, most often covalent chains, which extend along a particular lattice direction [6,7]. Some examples of these quasi-1D crystals include black phosphorus, SnSe, GaTe, InTe, and ReS_2 [8–12], which have attracted considerable attention owing to their in-plane anisotropic physical properties, including high electronic conductivity, thermal conductivity, and exciton recombination occurring only for a given lattice direction [10]. Such particular properties have prompted unconventional applications, such as polarization-sensitive photodetectors and thermoelectric devices [12,13]. As a consequence of their quasi-1D crystal structure, the electronic band structure of these materials typically combines the 2D-like thickness-dependent character along the z direction with inequivalent electronic dispersions along the x and y directions in the plane, bridging the gap between 2D and 1D materials such as nanowires, nanotubes, and other systems with a high geometrical aspect ratio [7].

Monotelluride compounds such as InTe and GaTe typically show a quasi-1D crystal structure, with weak out-of-plane bonding and anisotropic in-plane character [11]. However their environmental stability under ambient conditions is of concern, since other tellurium-based 2D materials such as $MoTe_2$ and WTe_2 are known to suffer rapidly from oxygen or moisture exposure [14,15]. As a consequence, the surface investigation of pristine InTe requires specific conditions, which we propose here to conduct using scanning tunneling microscopy (STM) operating in ultra-high-vacuum (UHV) conditions. STM has long been used to image the electronic structure of individual point defects in conductors, semiconductors, and ultrathin films [16]. Specific defects in InTe such as indium vacancies are known to form in the bulk and to

*meryem.bouaziz@universite-paris-saclay.fr
†abdelkarim.ouerghi@universite-paris-saclay.fr

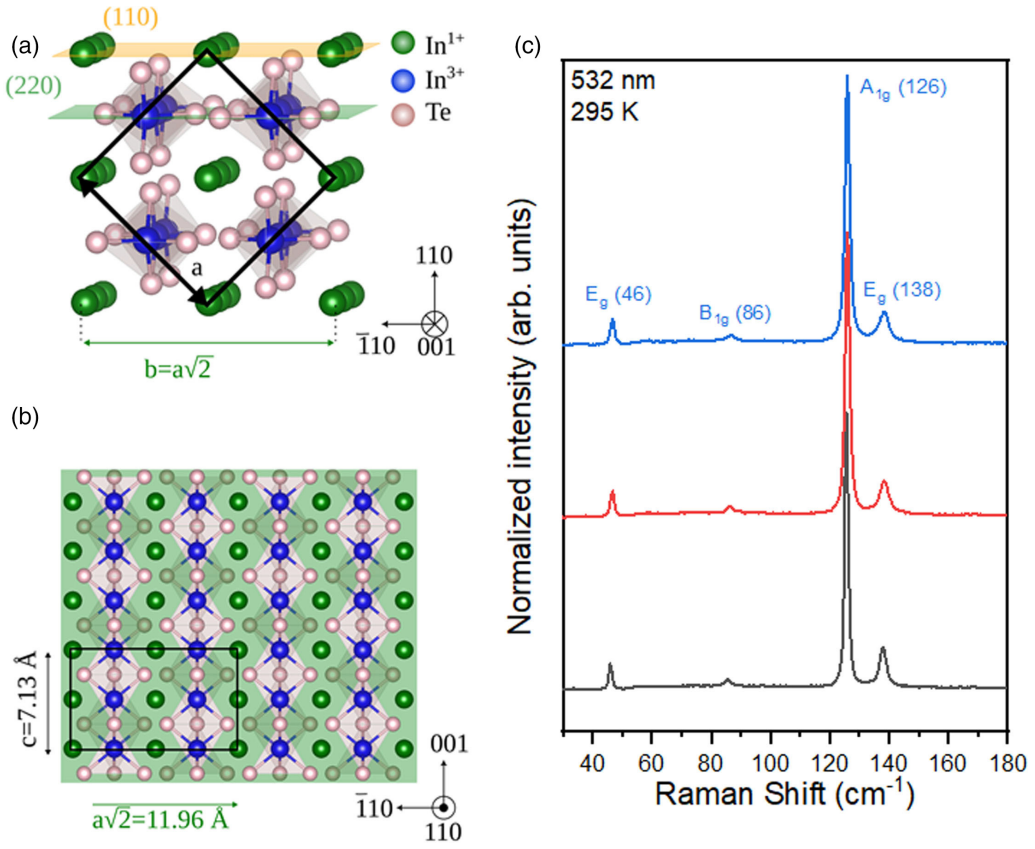

FIG. 1. Crystallographic and μ-Raman analysis of InTe. (a) Crystal structure of tetragonal InTe. In^{1+}, In^{3+}, and tellurium atoms are represented as green, blue, and pink spheres, respectively. The preferred 110 cleaving plane is indicated in light brown. The unit cell in marked by a black line. (b) Theoretical InTe (110) surface, exposing the In^{1+} atoms and the corresponding surface cell parameter. (c) Room-temperature μ-Raman spectra acquired from a different zone from a cleaved InTe (110) surface showing the three expected Raman lines: *Eg* at 48 cm^{-1} and 138 cm^{-1}, and the A_{1g} at 126 cm^{-1}.

affect thermoelectric properties [17,18]. In this context, the experimental surface characterization of the quasi-1D InTe surface and its associated defects is of interest, but is not yet reported in the literature.

Here we investigate the surface and electronic properties of InTe using STM and angle-resolved photoemission spectroscopy (ARPES). The crystalline nature of tetragonal InTe is first confirmed by STM, micro (μ)-Raman spectroscopy, and ARPES, with the expected natural cleavage plane corresponding to the (110) surface [10]. The ARPES data present a sharp band structure, indicative of the quality of the InTe crystal, but also a substantial p-type character. Further investigations by scanning tunneling spectroscopy (STS) identify specific defective regions, which impose particular electronic properties on InTe with respect to other defect-free areas. Comparison with the theoretical band structure and local density of state (LDOS) calculations using density functional theory (DFT) confirms the existence of in-gap states close to the valence band maximum (VBM), at the origin of the observed p-type character of InTe.

II. EXPERIMENTAL DETAILS

A. Photoemission spectroscopy

ARPES experiments were performed at the CASSIOPEE beamline of the SOLEIL synchrotron light source. The CASSIOPEE beamline is equipped with a Scienta R4000 hemispherical electron analyzer whose angular acceptance is ±15° (Scienta Wide Angle Lens). The valence band data were calibrated with respect to the Fermi level. High-quality samples from the "2D semiconductors" company were cleaved in UHV at a base pressure better than 1×10^{-10} mbar. The Fermi level was determined by fitting the leading edge of the gold crystal at the same photon energies and under the same experimental conditions. The experiment was performed at $T =$ 30 K. The incident photon beam was focused into a 50-μm spot (diameter) on the sample surface. All ARPES measurements were performed with a linear horizontal polarization.

B. Scanning tunneling microscopy

STM experiments are performed at 77 K using an LT-STM (Scienta-Omicron). The sample is prepared in the same conditions as ARPES measurements, cleaved at a base pressure better than 1×10^{-10} mbar and transferred immediately in the precooled STM head. STM images are acquired in the constant current mode.

C. μ-Raman measurements

The μ-Raman measurements were conducted at room temperature using a commercial confocal Horiba micro-Raman microscope with a ×100 objective and a 532-nm laser excita-

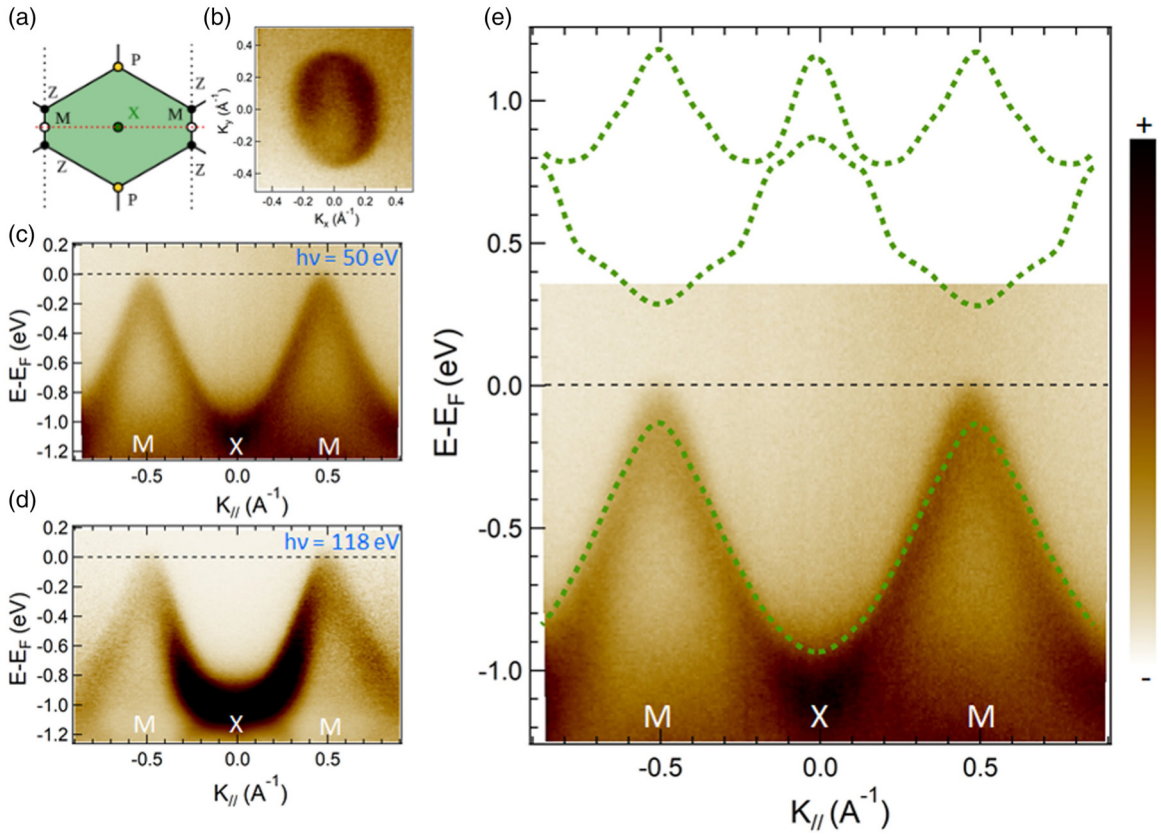

FIG. 2. (a) Projected Brillouin zone of InTe along the 110 axis. b) Isoenergic contour around the M point at −0.5 eV showing the 1D character of InTe (hυ = 50 eV). (c) and (d) Experimental ARPES dispersion of InTe along the MXM direction obtained with a photon energy of hυ = 50 eV and 118 eV, respectively. (d) ARPES data (hυ = 50 eV) superposed with theoretical DFT results computed with the HSE06 functional. The DFT bands are shifted to account for the Fermi-level position for the ARPES image.

tion. The laser beam was focused onto a small spot (diameter, ∼1 μm) on the sample.

III. RESULTS AND DISCUSSION

Bulk InTe is a tetragonal semiconductor that crystallizes in the TlSe structure under ambient conditions [19]. It is best described by the tetragonal space group $I4/mcm$, with the unit cell [Fig. 1(a), black line] being a right-angled cuboid with parameters $a = 8.444$ Å in the (100) and (010) directions while $a \neq c = 7.136$ Å along the [001] axis [17]. As-grown bulk InTe typically exhibits a p-type character [10,20]. While tellurium atoms solely occupy one crystallographic site ($8h$), indium atoms are distributed equally over two independent crystallographic sites—named hereafter In^{1+} and In^{3+}, respectively. The In^{3+} ions are tetrahedrally coordinated with tellurium atoms, forming covalent infinite edge-sharing tetrahedra along the c direction. Perpendicularly, along the [100] and [010] directions, those infinite $(InTe_2)^-$ covalent chains are weakly bonded to each other and intercalated by In^{1+} ions. These In^{1+} ions are actually surrounded by eight tellurium atoms in a tetragonal antiprismatic coordination, but show large atomic displacement values along the c direction, moving in a tunnel-like configuration between the covalently bound $(InTe_2)^-$ chains [10]. Due to the weak interactions between $(InTe_2)^-$ chains, the crystal tends to cleave along the (110) planes [20] [Fig. 1(a), light brown], cutting through the mobile In^{1+} positions. The exposed (110) surface shows a rectangular symmetry with parameter $a\sqrt{2}$ and c (Figure 1(b)). While the exposed In^{1+} atoms form a regular lattice of smaller parameter $a\sqrt{2}/2$ and $c/2$, the underlying tellurium atoms are positioned so that adjacent $(InTe_2)^-$ along [–110] chains are shifted by $c/2$ along [001] [see Fig. 1(a) and (b), (220) light-green plane), which requires boxing the entire surface cell. Representative Raman spectra acquired in three different zones (room temperature, 532-nm laser) from a freshly cleaved commercial InTe sample (2D Semiconductors) are shown in Fig. 1(c). All spectra expose identical Raman features with the same magnitude. The E_g (48 cm^{-1}, 138 cm^{-1}), B_{1g} (86 cm^{-1}), and A_{1g} (126 cm^{-1}) single modes are observed with frequencies that are in agreement with the literature on ambient tetragonal InTe [19,21], confirming the expected crystal structure and quality of our sample.

To resolve the previously described electronic properties of InTe, we have performed low-temperature ARPES measurements (30 K). In Fig. 2(a), we show the projected first Brillouin zone of InTe for the (110) surface. It exposes two inequivalent directions in reciprocal space that are perpendicular: $\overline{MXM}$, which is aligned with the real-space direction [–110] [i.e., across the $(InTe_2)^-$ chains], and $\overline{MZM}$ along [001] [i.e., along the $(InTe_2)^-$ chains], as expected from the anisotropic real-space symmetry [Figs. 1(a) and 1(b)]. In Fig. 2(b), we present the isoenergetic contours obtained at the M point (binding energy = −0.5 eV). The elliptical valley image is the result of anisotropy electronic properties of InTe.

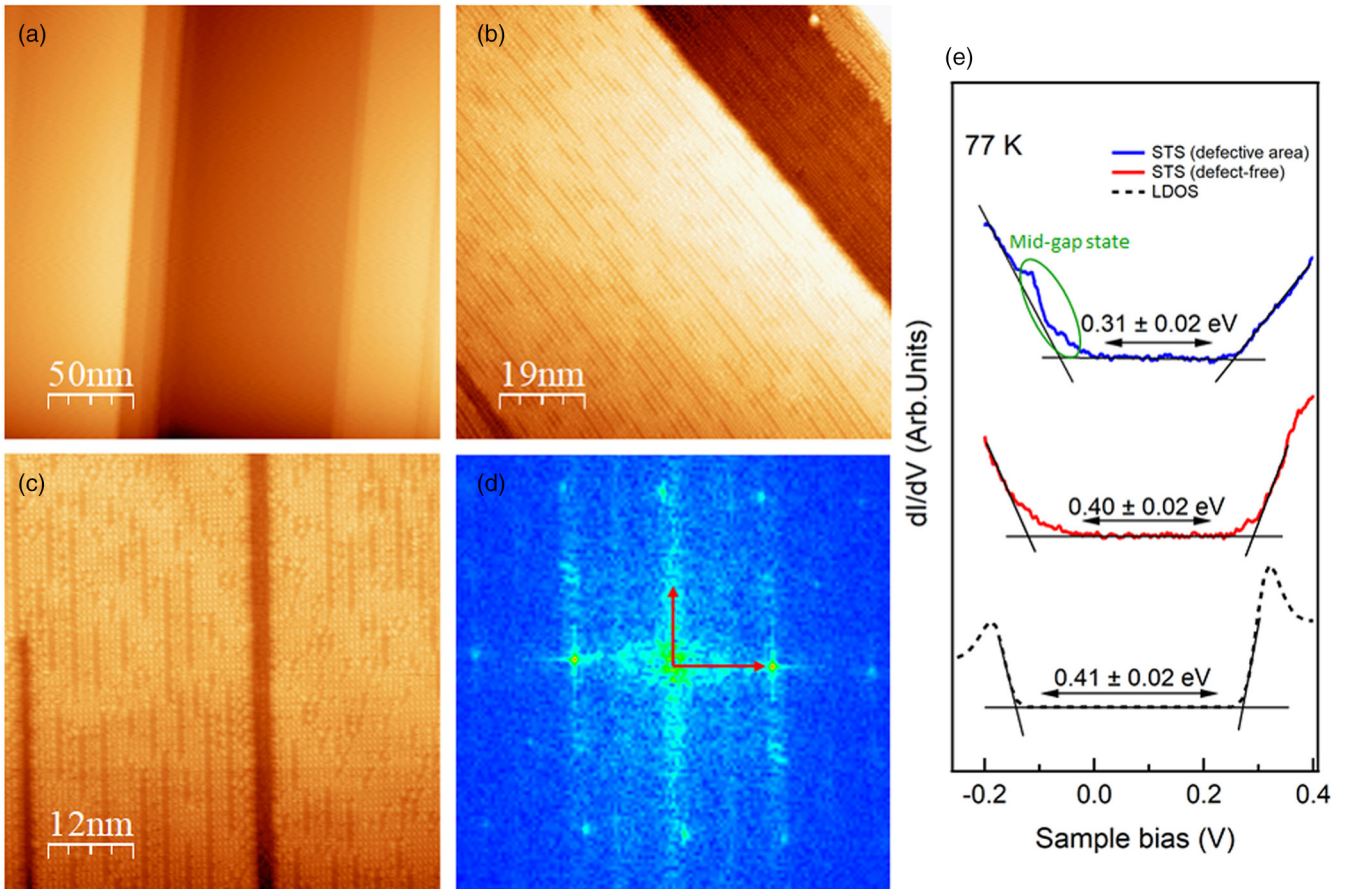

FIG. 3. Structural and electronic properties of InTe. (a) Large-scale STM image at 77 K of the UHV-cleaved surface of InTe revealing the oriented step edges on this surface ($V_{\text{bias}} = -0.5$ eV, $I_{\text{tunneling}} = 100$ pA). (b) and (c) Zoomed-in STM images, obtained with the same parameters, showing more linear features. (d) The corresponding FFT indicating the $a\sqrt{2} \times c$ periodicity of the InTe (110) surface. (e) The differential conductance (dI/dV) spectrum as a function of the bias voltage (red and blue curves), showing that the energy bandgap is $\sim 0.40 \pm 0.02$ eV. Total and partial electronic densities of states near the top of the valence band and the bottom of the conduction band of InTe (dashed black curve).

In Fig. 2(c) and (d), we report the experimental ARPES dispersion of the (110) InTe surface acquired along the $\overline{MXM}$ direction using a photon energy of 50 and 118 eV (surface and bulk sensitivity). The topmost part of the valence band is characterized by hole-like bands centered at the M point. The VBM at the M point of the Brillouin zone is mostly formed by p and s orbitals of tellurium and indium respectively, while at the X point the band is mostly composed by p orbitals of tellurium. We observe that the VBM is located at the Fermi level for the two-photon energy. This confirms the high p-type character of our InTe (110) bulk. Comparison with DFT calculations using the HSE06 functional [Fig. 2(e)] shows a good agreement. Considering the electronic bandgap of InTe calculated by Heyd-Scuseria-Ernzerhof, the VBM position indicates a p-type doping of InTe. This result confirms the strong p-type character of our InTe, in agreement with literature results on bulk InTe[10].

In order to determine the physical origin of the observed, strong p-type doping, we carried out a combined STM/STS study of the InTe (110) surface [7,22]. Figure 3(a) shows a large-scale topographic STM image of the UHV-cleaved surface of InTe, revealing wide terraces separated by high-density step edges and extended line defects aligned exclusively along a single in-plane direction, close to the vertical axis in Fig. 3(a). In zoomed-in STM images [Figs. 3(b) and 3(c)], we notice the ordered flat regions are better resolved and show finer features aligned along the same direction than the step edges. The corresponding fast Fourier transform [shown in Fig. 3(d)] reveals a clear rectangular symmetry, with the spacing along the vertical direction being close to that of the c-axis (8.0 Å) and the horizontal matching that of $a\sqrt{2} = (11.9$ Å). Comparison with the expected InTe (110) surface [Fig. 1(b)] confirms the surface orientation and cleavage plane, and determines the long axis of the step edges [large scale, Fig. 3(a)] and linear atomic features [small scale, Figs. 3(b) and 3(c)] to be the crystal c-axis. The absence of any other feature indicates that our InTe crystal is fully monocrystalline, without any rotational disorder, twinning domains, pits, or antiphase domain boundaries. The STM characterization of the InTe (110) surface strongly reflects the expected anisotropy of the InTe (110) and allows the direct imaging of 1D-like electronic features along the (in-plane) c-axis [10,19]. Figure 3(c) clearly shows that the InTe layer is incomplete, i.e., In^{1+} and $(InTe_2)^-$ ions are missing, which leads to the appearance of dark lines

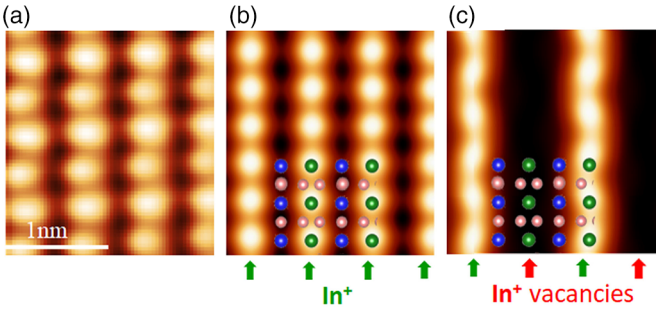

FIG. 4. Experimental and simulated STM images. (a) Experimental STM image of a fully In^{1+} terminated InTe (110) surface acquired using $U = 0.2$ V and $I = 100$ pA. (b) and (c) Simulated STM image of defect-free InTe and InTe with In^{+} defects taken at constant-height mode with $U = -1$ V and an STM tip 4.2 Å above the averaged InTe (110) surface. WSxM software was used for visualizing the image [30].

corresponding to holes. This suggests that single-atom vacancy defects on InTe can be formed. The density of In^{1+} vacancies is estimated to be about 20% to 40% of the area.

To investigate the electronic bandgap, complementary STS measurement at 77 K in defect-free (red spectrum) and defective (blue spectrum) areas, coupled with DFT calculations of LDOS [23] are presented in Fig. 3(e). The experimental differential conductance (dI/dV) spectroscopy versus bias voltage spectra is compared to the LDOS calculated by DFT. The theoretical LDOS of the InTe is very sharp at the top of the valence band and near the conduction band minimum, as well as for the experimental STS. The conduction band minimum is located at 0.28 ± 0.02 eV above the Fermi level, for both experimental spectra as well as for the calculated LDOS. However, a difference on the valence band side is noticed. The VBM is located at 0.12 ± 0.02 eV below the Fermi level (i.e., zero bias on the dI/dV spectra) in the defect-free area, while it is located near E_F for the spectrum measured on a defect. By comparing the two STS spectra (red and blue tank), we can see a difference in the VBM region. This difference can be associated with localized states in the gap of the sample near the VBM. The intrinsic electron quasiparticle bandgap is estimated at about $E = 0.40 \pm 0.02$ eV. This value is of the same range as the one obtained with the DFT (∼0.41 eV). The uncertainty in bandgap is the result of the lateral band-edge variations. The Fermi energy, corresponding to the zero bias in the dI/dV spectrum, is positioned near the VBM. As such, it suggests the presence of intrinsic charged defects in our specimens and a p-type doping, which we could relate to lattice vacancies or antisites responsible for p-doping in other 2D materials [24]. Still, the p-type character of our InTe (110) surface observed by STS agrees with our ARPES measurements.

In Fig. 4(a), we present a STM image of a particular area (defect free). We measure a spatial periodicity of $a\sqrt{2}/2 \times c/2$ in the perpendicular direction, which is consistent with the

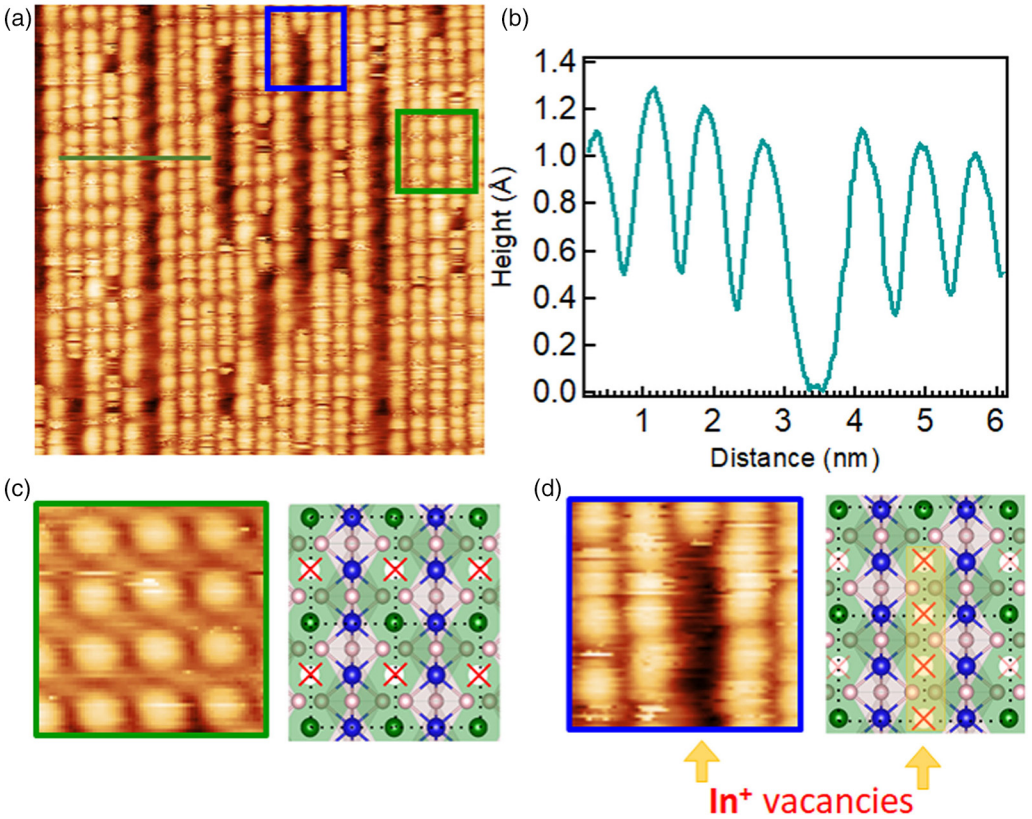

FIG. 5. Atomistic defects of the InTe (110) surface. (a) Atomically resolved STM topography (26×26 Å^2, $U = -0.5$ V, $I = 30$ pA). (b) Line profile across the chain. (c) Regular In^{1+} vacancy arrangement in a rectangular lattice. (d) Linear arrangement of In^{1+} vacancy forming an extended segment along the in-plane c-axis.

lattice parameters of the structure [Fig. 1(b)]. From the structural model, we attributed that the imaged bright spots to the In^{1+}. To verify our hypothesis, we have performed DFT calculations using the DFT local orbital molecular-dynamics code as implemented in Fireball [25–28]. We have optimized a 1×1 unit cell of fully In^{1+} terminated (defect free) InTe and InTe with In^{+} defects until the forces went below 0.1 eV $Å^{-1}$. A set of $8 \times 8 \times 1$ k-points has been used for both structural optimization and DOS calculations. STM simulations have been performed within a Keldysh-Green function formalism as described in Ref. [29] On the other hand, the tip is modeled by a W-pyramid of five atoms coupled to four layers of W(100) with a 5×5 periodicity. WSxM software has been used for image visualization [30]. In Figs. 4(b) and 4(c), we present two simulated STM images (InTe defect free and InTe with In^{+} defects), constructed with the same parameters as our STM experimental conditions. We observe a good match between the experimental and simulated STM image of defect-free InTe (110) [Figs. 4(a) and 4(b)]. Based on DFT calculations, we confirm the direct observation of one-dimensional In^{1+} chains in an InTe [Fig. 4(a)]. The superposed crystal lattice from DFT [Fig. 4(b), insert] confirms that the observed protrusions localize close to the In^{1+} atomic positions.

For the defective InTe, the calculated STM image [Fig. 4(c)] shows the In^{1+} vacancy as a depression, which is similar to the experimental observation [Fig. 3(c)]. The topographic signature of these defects is imaged using STM, showing the In^{1+} vacancies as depressions on the InTe surface—notably, extended vacancy lines along the crystal c-axis. If we refer to Fig. 3(c), we now interpret the line defect to be In^{1+} defective. Our STM/STS and ARPES results thus demonstrate such In^{1+} vacancies are responsible for the p-type character of InTe and, more generally, are a typical feature of TlSe-like materials [10].

We now turn to the detailed investigation of the InTe (110) with In^{1+} defects in order to study the atomic structure of the observed 1D line features. Figure 5(a) shows an atomically resolved STM image of the InTe (110) surface. The crystal c-axis is vertical, and the corresponding chain-like features are now obvious. However, we note that each 1D chain presents a slightly different structure along its axis than its neighbors, alternating short, long protrusions or gaps. The height profile perpendicular to the chains [Fig. 5(a), blue line] is shown in Fig. 5(b). The oscillation period is $a\sqrt{2}/2$ ($\sim$6 Å) and the depth is about 1 Å. This vertical distance corresponds to the vertical distance between the top In^{1+} atoms and the underlying In^{3+} atoms. The lateral period also matches the expected In^{1+} position, with a spacing of $a\sqrt{2}/2$ [Fig. 1(b)] along the -110 direction. Given that the InTe (110) surface is obtained by mechanical cleaving through the In^{1+} (110) plane, we suggest some vacancy in the exposed In^{1+} layer at the top surface. In Fig. 5(c) (left), we investigate a small regular array characterized by a lateral length of $a\sqrt{2}/2$, but with a double vertical period (7 Å) equal to cell parameter c. Following our hypothesis, this situation corresponds to a regular reconstruction of the surface with half of the In^{1+} atoms missing [Fig. 5(c), right]. Another variant is presented Fig. 5(d) (left), in which a typical extended 1D defect is shown and which we interpret as In^{1+} vacancies aligned along the c-axis [Fig. 5(d), right]. This surface model with mobile In^{1+} vacancies is also compatible with the overall picture shown in Fig. 5(a). This spatial distribution of In^{1+} vacancies is random and creates various combinations of regular arrays ($a\sqrt{2}/2 \times c$, $\sim$ 40% In^{1+} vacancies), vacancy lines, or less ordered arrangements.

IV. CONCLUSION

In summary, we have combined complementary techniques to investigate the structural and electronic properties of the cleaved surface of quasi-1D InTe. Our combined DFT and STM study confirms the (110) preferential cleaving plane and reveals various surface organization of In^{1+} vacancies, sometimes arranged in a regular array but mostly in extended segments along the in-plane c-axis. These In^{1+} vacancies are the dominant defects in InTe, and the STS results indicate that they are responsible for the strong p-type doping of InTe, as also observed using ARPES. Further investigation of these In^{1+} vacancies offers insight into alternative doping strategies, possibly by substitution, to obtain opposite n-type electrical conduction while maintaining the inherent, strong anisotropy of InTe.

ACKNOWLEDGMENTS

We acknowledge the financial support by MagicValley (Grant No. ANR-18-CE24-0007) and Graskop (Grant No. ANR-19-CE09-0026), 2D-on-Demand (Grant No. ANR-20-CE09-0026), and MixDferro (Grant No. ANR-21-CE09-0029), the French technological network RENATECH. This work is also supported by a public grant overseen by the French National Research Agency (ANR) as part of the "Investissements d'Avenir" program (Labex NanoSaclay, Grant No. ANR-10-LABX-0035) and by the French technological network RENATECH. C.G. thankfully acknowledges the computer resources at Altamira, the technical support provided by the Physics Institute of Cantabria (IFCA) of the University of Cantabria (Project No. FI-2022-3-0021), and the financial support by the Spanish Science and Innovation Ministry (Project No. PID2021-123112OB-C21).

The authors declare no competing interests.

APPENDIX

Figure 6 presents the ARPES dispersion of the (110) InTe surface acquired along the $\overline{MXM}$ direction using a photon energy of 84 eV.

The energy distribution curves (EDCs) of the valence band, measured with a photon energy of 50 and 118 eV, are shown in Fig. 7 (green and red lines). On the same graph, the Fermi edge of a clean gold sample measured in the same experimental conditions is presented (blue line). The zero of the binding energy (i.e., the Fermi level) was taken at the leading edge of this gold sample.

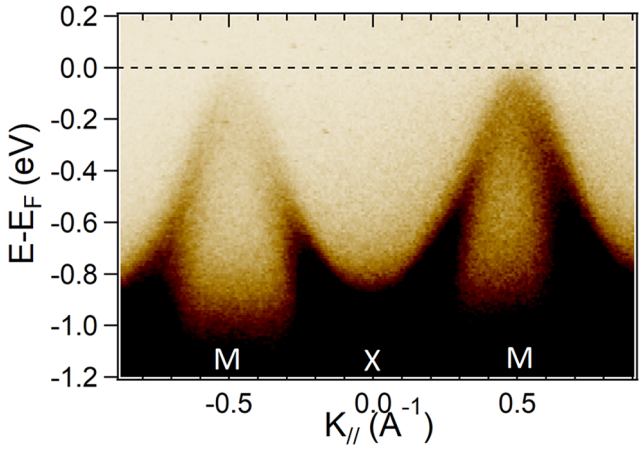

FIG. 6. Experimental ARPES dispersion of InTe along the *MXM* direction obtained with a photon energy of $h\upsilon = 84$ eV.

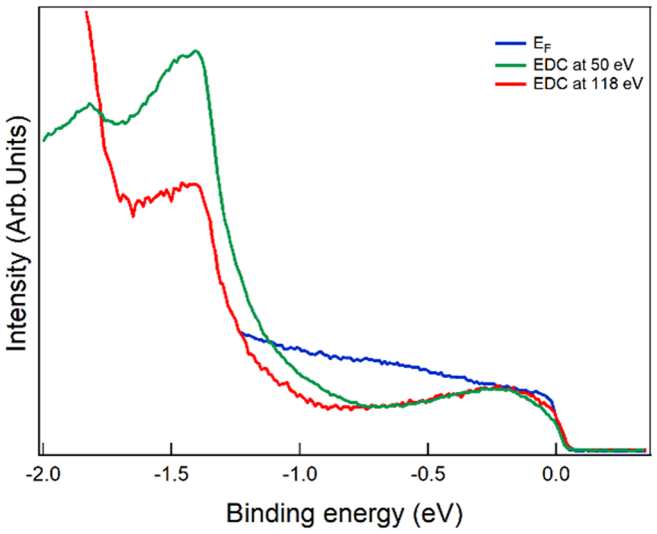

FIG. 7. EDCs extracted from ARPES measurements at 50 eV (green line) and 118 eV (red line). The blue curve is the Fermi edge of a clean gold sample measured in the same experimental conditions.

[1] Y.- C. Lin *et al.*, Direct synthesis of van der Waals solids, ACS Nano **8**, 3715 (2014).

[2] A. K. Geim and K. S. Novoselov, The rise of graphene, Nat. Mater. **6**, 183 (2007).

[3] A. K. Geim, Graphene: Status and prospects, Science **324**, 1530 (2009).

[4] A. K. Geim and I. V Grigorieva, Van der Waals heterostructures, Nature (London) **499**, 419 (2013).

[5] Z. Ben Aziza *et al.*, Van der Waals epitaxy of GaSe/graphene heterostructure: Electronic and interfacial properties, ACS Nano **10**, 9679 (2016).

[6] Z. Gao, T. Zhu, K. Sun, and J.-S. Wang, Highly anisotropic thermoelectric properties of two-dimensional As_2Te_3, ACS Appl. Electron. Mater. **3**, 1610 (2021).

[7] L. Khalil *et al.*, Electronic band gap of van der Waals α-As_2Te_3 crystals, Appl. Phys. Lett. **119**, 043103 (2021).

[8] J. M. Gonzalez and I. I. Oleynik, Layer-dependent properties of SnS_2 and $SnSe_2$ two-dimensional materials, Phys. Rev. B **94**, 125443 (2016).

[9] F. Wang *et al.*, Tunable GaTe-MoS_2 van der Waals p-n junctions with novel optoelectronic performance, Nano Lett. **15**, 7558 (2015).

[10] J. Zhang *et al.*, Direct observation of one-dimensional disordered diffusion channel in a chain-like thermoelectric with ultralow thermal conductivity, Nat. Commun. **12**, 6709 (2021).

[11] S. Pal and D. N. Bose, Growth, characterisation and electrical anisotropy in layered chalcogenides GaTe and InTe, Solid State Commun. **97**, 725 (1996).

[12] J. Shim *et al.*, Phosphorene/rhenium disulfide heterojunction-based negative differential resistance device for multi-valued logic, Nat. Commun. **7**, 13413 (2016).

[13] A. Pant *et al.*, Fundamentals of lateral and vertical heterojunctions of atomically thin materials, Nanoscale **8**, 3870 (2016).

[14] I. G. Lezama *et al.*, Indirect-to-direct band gap crossover in few-layer $MoTe_2$, Nano Lett. **15**, 2336 (2015).

[15] S. Tang *et al.*, Quantum spin Hall state in monolayer 1T′-WTe_2, Nat. Phys. **13**, 683 (2017).

[16] B. Lalmi *et al.*, Flower-shaped domains and wrinkles in trilayer epitaxial graphene on silicon carbide, Sci. Rep. **4**, 4066 (2014).

[17] S. Y. Back *et al.*, Temperature-induced Lifshitz transition and charge density wave in $InTe_{1-\delta}$ thermoelectric Mater., ACS Appl. Energy Mater. **3**, 3628 (2020).

[18] S. Misra *et al.*, Enhanced thermoelectric performance of InTe through Pb doping, J. Mater. Chem. C **9**, 14490 (2021).

[19] S. Misra *et al.*, Reduced phase space of heat-carrying acoustic phonons in single-crystalline InTe, Phys. Rev. Res. **2**, 043371 (2020).

[20] S. Misra *et al.*, Synthesis and physical properties of single-crystalline InTe: Towards high thermoelectric performance, J. Mater. Chem. C **9**, 5250 (2021).

[21] V. Rajaji, K. Pal, S. Ch. Sarma, B. Joseph, S. C. Peter, U. V. Waghmare, and C. Narayana, Pressure induced band inversion, electronic and structural phase transitions in InTe: A combined experimental and theoretical study, Phys. Rev. B **97**, 155158 (2018).

[22] H. Henck *et al.*, Evidence of direct electronic band gap in two-dimensional van der Waals indium selenide crystals, Phys. Rev. Mater. **3**, 034004 (2019).

[23] D. Pierucci *et al.*, Evidence for flat bands near the Fermi level in epitaxial rhombohedral multilayer graphene, ACS Nano **9**, 5432 (2015).

[24] D. Pierucci *et al.*, Evidence for highly p-type doping and type II band alignment in large scale monolayer WSe_2/Se-terminated GaAs heterojunction grown by molecular beam epitaxy, Nanoscale **14**, 5859 (2022).

[25] J. P. Lewis *et al.*, Advances and applications in the FIREBALL *ab initio* tight-binding molecular-dynamics formalism, Phys. Status Solidi Basic Res. **248**, 1989 (2011).

[26] O. F. Sankey and D. J. Niklewski, *Ab initio* multicenter tight-binding model for molecular-dynamics simulations and other applications in covalent systems, Phys. Rev. B **40**, 3979 (1989).

[27] P. Jelínek, H. Wang, J. Lewis, O. Sankey, and J. Ortega, Multicenter approach to the exchange-correlation interactions in *ab initio* tight-binding methods., Phys. Rev. B **71**, 235101 (2005).

[28] M. A. Basanta, Y. J. Dappe, P. Jelínek, and J. Ortega, Optimized atomic-like orbitals for first-principles tight-binding molecular dynamics, Comput. Mater. Sci. **39**, 759 (2007).

[29] C. González, E. Abad, Y. J. Dappe, and J. C. Cuevas, Theoretical study of carbon-based tips for scanning tunnelling microscopy, Nanotechnology **27**, 105201 (2016).

[30] I. Horcas *et al.*, WSXM: A software for scanning probe microscopy and a tool for nanotechnology, Rev. Sci. Instrum. **78**, 013705 (2007).